Insight into Eu redox and Pr^{3+} 5d emission in $KSrPO_4$ by VRBE scheme construction

Zhou, Rongfu; Lin, Litian; Liu, Chunmeng; Dorenbos, Pieter; Tao, Ye; Huang, Yan; Liang, Hongbin

DOI
10.1039/c7dt03813e

Publication date
2018

Document Version
Accepted author manuscript

Published in
Dalton Transactions

Journal Name

ARTICLE

Insight into Eu redox and Pr^{3+} 5d emission in $KSrPO_4$ by VRBE scheme construction†

Received 00th January 20xx,
Accepted 00th January 20xx

DOI: 10.1039/x0xx00000x

www.rsc.org/

Rongfu Zhou,[a] Litian Lin,[a] Chunmeng Liu,[a] Pieter Dorenbos,[b] Ye Tao,[c] Yan Huang[c] and Hongbin Liang[a,*]

Series of Ln-doped $KSrPO_4$ (Ln = Ce^{3+}, Eu^{3+}, Eu^{2+}, Pr^{3+}) phosphors are prepared through a high-temperature solid-state method. The $KSrPO_4$ compound is confirmed to be β-K_2SO_4 structure with *Pnma* group by Rietveld refinement, and the temperature-dependent lattice parameters are investigated with the powder X-ray diffraction results at different temperatures. Ce^{3+} and Eu^{3+} ions are introduced to probe the crystal field strength (CFS) and the lanthanide site symmetry by VUV-UV-vis spectroscopy. The temperature-dependent luminescence properties of $KSrPO_4$: Ce^{3+}/Eu^{2+} exhibit excellent thermal stability of Ce^{3+}/Eu^{2+} luminescence. Based on the VUV-UV-vis spectra of Ce^{3+} and Eu^{3+} doped $KSrPO_4$, the vacuum referred binding energy (VRBE) scheme is constructed to understand the redox properties of Eu, the 5d energy levels of Pr^{3+} and thermal quenching characteristics of Ce^{3+} and Eu^{2+} luminescence.

1. Introduction

Eu^{2+}-activated luminescent materials have drawn wide attention because of their importance in solid-state lighting and displays.[1-4] The preparation of divalent europium doped materials often needs reducing conditions, for example, H_2 or CO ambiance, etc. But in some special cases, Eu^{2+} can also be (partially) obtained through a solid-state reaction approach with Eu(III)-containing raw materials in non-reducing conditions.[5,6] This is, of course, the result of composition and structure of these special host compounds. From the viewpoint of electron transfer, the redox processes of Eu^{3+} and Eu^{2+} as dopants in solid state inorganic compounds relate to factors such as the electronic structure of conduction band and valence band, the band gap energy and the Femi level of the host compound, the 5d energy of Eu^{2+}, and the energy of charge transfer state (CTS) between Eu^{3+} and coordinated atoms.[7] Clear understanding of the redox behaviour of Eu^{2+} / Eu^{3+} in different host compounds is a key issue for the preparation and application of Eu^{2+}-activated luminescent materials.

Eu^{2+}, Pr^{3+} and Ce^{3+} doped luminescent materials are also applied as important scintillators. SrI_2: Eu^{2+}, and LnX_3: Ce^{3+} (Ln = La, Lu; X = Br, I) are commercially available scintillators in various detecting areas.[8-10] These applications are benefited from the typical parity-allowed 5d-4f transitions of these ions and therefore with fast radiative rates. In the same site of the same host compound, fluorescence decay of Pr^{3+} is usually faster than that of Ce^{3+} or Eu^{2+} due to its shorter emission wavelength.[11] Therefore Pr^{3+} is an important activator in fast decay scintillators. Because the binding energy of outer 5d electrons is highly sensitive to the local coordination environment of the host lattice, it is essential to fully understand the energy and thermal stability of d-f emission of Pr^{3+} in various host compounds to find novel Pr^{3+} doped scintillation materials.

The compound $KSrPO_4$ is one of the $ABPO_4$ (A = monovalent cations, B = divalent cations) monophosphates with tetrahedral rigid anion groups.[12] And Eu^{2+}, Tb^{3+}, $Sm^{2+/3+}$ doped $KSrPO_4$ phosphors exhibit excellent luminescence properties.[13-15] In this paper, we investigate the temperature- and doping concentration- dependent synchrotron radiation VUV-UV-vis luminescence spectra of Ce^{3+}, Pr^{3+}, Eu^{3+} and Eu^{2+} doped $KSrPO_4$. Especially, the electronic scheme with the vacuum referred binding energies (VRBE) for all lanthanide ions is constructed based on measured band gap energy, 5d orbital energies of Ce^{3+} and Eu^{3+}-O^{2-} charge transfer energy with the purpose to understand the excellent thermal stabilities of luminescence of Ce^{3+} and Eu^{2+}, the 5d energy of Pr^{3+} and the redox of Eu. Eu-doped samples are prepared in inert N_2, oxidizing air and reducing CO conditions to get clearer insight into the redox characteristics of Eu in $KSrPO_4$. The work demonstrates a convenient approach to predict the stability of dopant Eu^{2+} / Eu^{3+} and the energy of d-f emission of Pr^{3+} in a specific host compound.

[a] *MOE Key Laboratory of Bioinorganic and Synthetic Chemistry, KLGHEI of Environment and Energy Chemistry, School of Chemistry, Sun Yat-sen University, Guangzhou 510275, China.*
[b] *Faculty of Applied Sciences, Delft University of Technology, Mekelweg 15, 2629 JB Delft, The Netherlands.*
[c] *Beijing Synchrotron Radiation Facility, Institute of High Energy Physics, Chinese Academy of Sciences, Beijing 100039, China.*
* E-mail: cesbin@mail.sysu.edu.cn; Tel.: +86 20 84113695.
† Electronic Supplementary Information (ESI) available: [details of any supplementary information available should be included here]. See DOI: 10.1039/x0xx00000x

2. Experimental

Ln-doped $KSrPO_4$ (Ln = Ce^{3+}, Eu^{3+}, Eu^{2+}, Pr^{3+}) samples are prepared using a conventional solid-state reaction route. The analytic reagents $SrCO_3$, K_2CO_3, $NH_4H_2PO_4$ and 99.99% pure rare-earth oxides Eu_2O_3, CeO_2, Pr_6O_{11} are used as starting materials. These reactants are thoroughly ground in an agate mortar and pre-fired at 975 K in air atmosphere for 5 h. Then Ce^{3+} or Pr^{3+} doped samples are annealed at 1570 K for 3 h under CO ambiance which are produced from the incomplete combustion of carbon at high-temperature. Europium doped sample batches with each a specific concentration are divided into three parts and fired in reducing CO, inert N_2, or oxidizing air flow, respectively. Finally, the samples are cooled to RT by switching off the muffle furnace and ground into powders for subsequent analysis.

The phase purity of the samples is estimated by powder X-ray diffraction (P-XRD) on a Bruker D8 advanced X-ray diffractometer with a wavelength of 1.54056 Å Cu Kα radiation at 40 kV and 40 mA, demonstrating no detectable impurity phase in all samples. High quality P-XRD data for the refinement are collected within the 2θ range from 7° to 110° at a 2θ step of 0.02°. The Rietveld refinement is performed using the TOPAS - Academic program.[16]

The UV-vis excitation and emission spectra as well as the luminescence decay curves are recorded at an Edinburgh FLS 920 combined fluorescence lifetime and steady-state spectrometer equipped with a thermo-electronic cooled (-19.5 °C) Hamamatsu R928P Model photomultiplier. The 450 W xenon lamp is used as the excitation source of steady-state excitation and corresponding emission spectra. A 150 W nF900 lamp with a pulse width of 1 ns and a 60 W μF flash lamp with a pulse width of 1.5-3.0 μs are used for the measurements of decay curves. The temperature dependent spectral measurements at 77-500 K range are performed by putting the samples in a liquid nitrogen cooling OptistatDN2 cryostat and controlled by an Oxford MercuryiTC temperature controller. The excitation and emission spectra in the VUV-UV range are measured on the beam line 4B8 of the Beijing Synchrotron Radiation Facility (BSRF) under normal operating conditions using the spectrum of sodium salicylate (o-$C_6H_4OHCOONa$) as a standard.[11,17]

3. Results and discussion

3.1. Structure and Phase Characterization

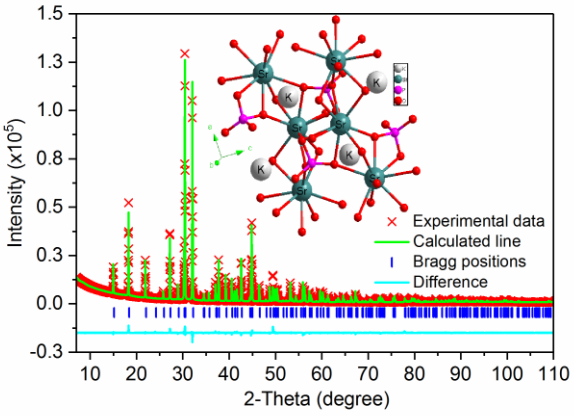

Fig. 1 Experimental (red crosses) and calculated (green solid line) XRD patterns, their difference (cyan solid line), and the Bragg reflection positions (blue ticks) of $KSrPO_4$; the inset shows the crystal structure of $KSrPO_4$.

Fig. 1 shows Rietveld refinement results based on laboratory P-XRD data of the synthesized $KSrPO_4$ compound using the *Pnma* structure model.[18,19] No impurity peak is observed, and the obtained reliability factors R_{wp}, R_p and R_B are 5.89%, 3.57%, and 5.92%, respectively. The final refined structural parameters are listed in ESI Table S1†. The $KSrPO_4$ compound is crystallized in an orthorhombic structure with space group *Pnma*. The lattice parameters are a = 7.34706(4) Å, b = 5.55249(3) Å, c = 9.61716(6) Å and V = 392.325(4) $Å^3$. The inset of Fig. 1 depicts the crystal structure of $KSrPO_4$. A Sr^{2+} atom is coordinated by nine oxygen atoms with C_s point symmetry. The average bond length between Sr^{2+} and O^{2-} is ~2.688 Å (ESI Table S2†) and the nearest distance of two adjacent Sr^{2+} ions is ~3.809 Å. The polyhedral SrO_9, KO_{10} and PO_4 form the framework of $KSrPO_4$ structure by sharing their corner or edges. The ESI Fig. S1† shows the representative P-XRD patterns of Ce^{3+}, Eu^{3+}, Pr^{3+} and Eu^{2+} singly doped $KSrPO_4$ samples. All XRD patterns are in good agreement with the refined $KSrPO_4$ result, implying that all samples are of single pure phase and the doping of Ce^{3+} / Eu^{3+} / Pr^{3+} / Eu^{2+} ions do not significantly influence the diffractogram of the host compound. Due to the more suitable ionic size and valence state [r(Ce^{3+}) = 1.336 Å, r(Eu^{3+}) = 1.26 Å, r(Pr^{3+}) = 1.319 Å, r(Eu^{2+}) = 1.44 Å, r(Sr^{2+}) = 1.45 Å; coordination number = 9][20], Ce^{3+}, Eu^{3+}, Pr^{3+} and Eu^{2+} may prefer occupying the Sr^{2+} site when doped into $KSrPO_4$.

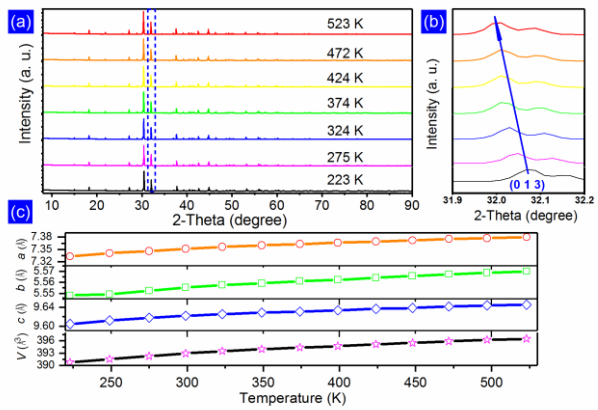

Fig. 2 (a) Temperature-dependent P-XRD patterns of $KSrPO_4$ in the temperature range of 223-523 K; (b) magnified P-XRD patterns (31.9-32.2 degree of 2-theta) of $KSrPO_4$; (c) lattice parameters *a*, *b*, *c* and *V* of $KSrPO_4$ as a function of temperature.

To study the thermal evolution of the host structure, Fig. 2 (a) displays P-XRD patterns of $KSrPO_4$ at temperatures from 223 to 523 K. $KSrPO_4$ maintains the orthorhombic structure (space group *Pnma*) in the investigated temperature range. The magnified patterns from 31.9 to 32.2 degree of 2-theta in Fig. 2 (b) shows that the diffraction peaks slightly shift to the lower angle side, which implies that the unit cell of the host undergoes a thermal expansion. Based on these XRD patterns, the lattice constants can be calculated by Rietveld refinement. As displayed in Fig. 2 (c), the lattice parameters *a*, *b*, *c* and *V* are found to increase with rising temperature, which may affect the luminescence properties of samples as discussed later.

3.2. Luminescence of Ce^{3+} in $KSrPO_4$

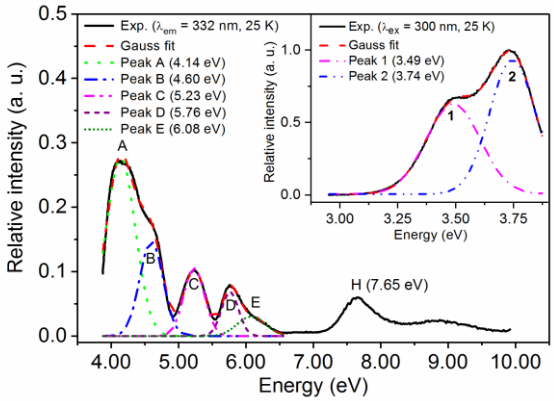

Fig. 3 Synchrotron radiation VUV-UV excitation (λ_{em} = 332 nm) spectrum of $K_{1.001}Sr_{0.998}Ce_{0.001}PO_4$ at 25 K and corresponding Gaussian fitting results; the inset shows the emission (λ_{ex} = 300 nm) spectrum at 25 K and the fitting results.

Fig. 3 shows the VUV-UV excitation (λ_{em} = 332 nm) spectrum of the sample with nominal composition $K_{1.001}Sr_{0.998}Ce_{0.001}PO_4$ at 25 K. The high-lying excitation band with a maximum at about 7.65 eV (band H) is attributed to the excitonic absorption of the $KSrPO_4$ host. The absorptions below ~6.50 eV are assigned to the f-d excitation bands of Ce^{3+} in $KSrPO_4$. In this range three clear bands A, C, and D can be observed. The bands A and D have shoulder bands B and E at their higher energy sides, respectively. When we assume that Ce^{3+} ions occupy nine-fold coordinated Sr^{2+} sites with a low symmetry C_s group, the 5d orbitals of Ce^{3+} should be split into five non-degenerated orbitals. Therefore, the excitation curve in the 3.87-6.55 eV (190-320 nm) spectral range is fitted by a sum of five Gaussian functions to estimate the energies of 4f-5d transitions of Ce^{3+}. These energies are at about 4.14 (A), 4.60 (B), 5.23 (C), 5.76 (D), and 6.08 (E) eV, respectively. Consequently, the centroid energy of Ce^{3+} 5d states, viz. the arithmetic mean energy of the five f-d excitation bands, is calculated to be about 5.16 eV, meaning that the down-shift of centroid energy of Ce^{3+} 5d state (ε_c) in $KSrPO_4$ is about 1.19 eV with respect to that of free gaseous Ce^{3+} (6.35 eV). This value is near those of other phosphates, such as $K_3Lu(PO_4)_2$ (1.17 eV),[21] YPO_4 (1.19 eV),[21] $Ca_9Y(PO_4)_7$ (1.20 eV),[22] and $LuPO_4$ (1.20 eV),[21] which implies that Ce^{3+} ions in these phosphate compounds have nearly same nephelauxetic effect, covalence or spectroscopic polarization.[21,23] Meanwhile, the experimental crystal field splitting of Ce^{3+} in $KSrPO_4$ is calculated to be approximately 1.94 eV by subtracting the energy of the first 5d orbital (4.14 eV) from that of the fifth 5d one (6.08 eV). This value is in the range of those of Ce^{3+} in compounds SrB_4O_7 (1.66 eV),[24] $Sr_2Mg(BO_3)_2$ (2.10 eV),[25] and $SrAl_2O_4$ (2.68 eV, 2.75 eV),[26] in which Ce^{3+} ions occupy nine-fold Sr^{2+} sites with C_s or C_1 symmetry.

The emission (λ_{ex} = 300 nm) spectrum of $K_{1.001}Sr_{0.998}Ce_{0.001}PO_4$ at 25 K is fitted using a sum of two Gaussian components as displayed in the inset of Fig. 3. The obtained two bands (1, ~3.49 eV; 2, ~3.74 eV) are originated from the transitions from the lowest 5d state to its ^2F_J (J = 7/2, 5/2) 4f ground state of Ce^{3+}, respectively. Their energy difference is evaluated about 0.25 eV (2.02×10^3 cm^{-1}), which is coincident with the theoretical energy difference of ^2F_J (J = 5/2, 7/2) multiplets (~2.00×10^3 cm^{-1}). According to the energy difference between the band peaks of the lowest 5d and $^2F_{5/2}$ transition in excitation and emission spectra, the Stokes shift of Ce^{3+} is approximately 0.40 eV (~3.23×10^3 cm^{-1}). Stokes shift is related to Huang-Rhys parameter and effective phonon energy and depends on the characteristic of material. The value in present case is close to that in other monophosphates, such as $NaCaPO_4$ (0.38 eV), and $LiSrPO_4$ (0.40 eV).[27,28] The ESI Fig. S2† shows the highest-height normalized VUV-UV excitation (λ_{em} = 332 and 354 nm) and emission (λ_{ex} = 200, 215, 235, 270 and 300 nm) spectra of sample $K_{1.001}Sr_{0.998}Ce_{0.001}PO_4$ at 25 K. The excitation spectra by monitoring different emission wavelengths overlap to each other, and the emission spectra under different wavelength excitation also have the similar profiles. These phenomena demonstrate that the sample is without impurity phase and reveal the occurrence of only one

kind of Ce^{3+} luminescence center in the sample as we mentioned above. The luminescence decay curves at different wavelength conditions in ESI Fig. S3† further confirm this result. They all possess the same exponential decay properties and the lifetime of Ce^{3+} in $KSrPO_4$ is evaluated about 25.7 ns.

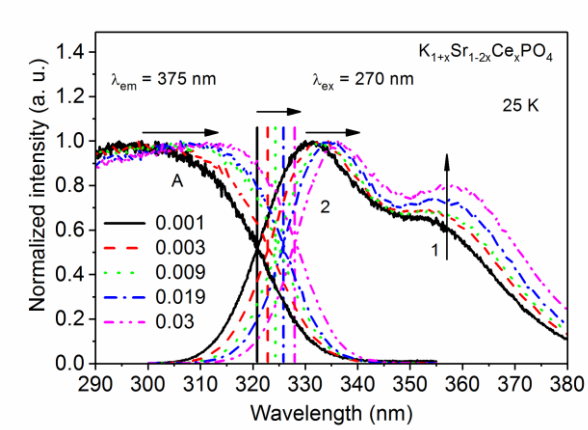

Fig. 4 Height-normalized excitation (λ_{em} = 375 nm) and emission (λ_{ex} = 270 nm) spectra of samples $K_{1+x}Sr_{1-2x}Ce_xPO_4$ (x = 0.001, 0.003, 0.009, 0.019 and 0.03) in 290-380 nm range at 25 K.

The height-normalized excitation (λ_{em} = 375 nm) and emission (λ_{ex} = 270 nm) spectra of samples $K_{1+x}Sr_{1-2x}Ce_xPO_4$ (x = 0.001, 0.003, 0.009, 0.019 and 0.03) are plotted in Fig. 4. With increasing Ce^{3+} content, excitation band of 4f-5d_1 transition and emission spectra gradually shift to lower energies, and the intensity of 5d_1-$^2F_{7/2}$ emission increases with respect to that of 5d_1-$^2F_{5/2}$. Since smaller Ce^{3+} ion occupy larger Sr^{2+} site, the lattice may experience a little contraction and the CFS around Ce^{3+} becomes larger, which pushes the 5d_1 level towards lower energies. The zero phonon line (ZPL) position directly indicates the energy of the 4f-5d_1 transition of Ce^{3+}. Its position can be estimated as the intersection point of the excitation and emission spectra, although we did not observe ZPLs in the spectra.[29] Fig. 4 shows the red shift of the intersection point with increasing Ce^{3+} doping, indicating that ZPLs shift to lower energies with stronger CFS around Ce^{3+}. Accordingly, the emission peaks of Ce^{3+} gradually shift to longer wavelengths. Moreover, in consideration of the significant overlap between excitation and emission spectra, the self-absorption effect of Ce^{3+} is also active in our case. This effect also shifts the emission band to the lower energy side in some extent, and meanwhile gives rise to the decrease of relative intensity of 5d_1-$^2F_{5/2}$ emission.[11,29] Therefore, the relative intensity of 5d_1-$^2F_{7/2}$ emission looks like stronger in height-normalized spectra. The ESI Fig. S4† (a) shows the concentration-dependent emission spectra of $K_{1+x}Sr_{1-2x}Ce_xPO_4$ (x = 0.001, 0.003, 0.009, 0.019 and 0.03) samples under 270 nm excitation at RT. With increase of doping contents, emission intensities of Ce^{3+} increase gradually, demonstrating that concentration quenching does not occur in this concentration range. The luminescence decay curves (λ_{ex} = 290 nm, λ_{em} = 354 nm) of samples are shown in ESI Fig. S4† (b). All curves follow the exponential characteristic and overlapped with each other, further confirming that concentration quenching of Ce^{3+} emission does not occur until x = 0.03.

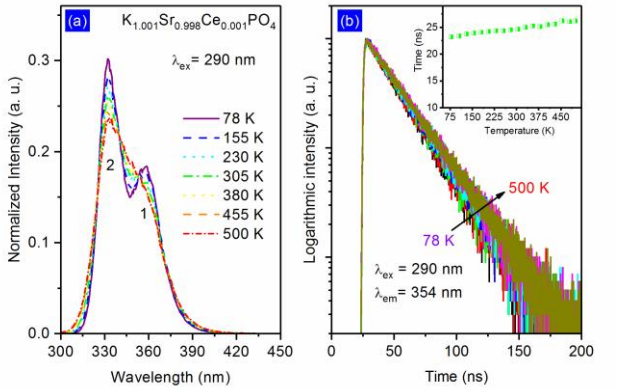

Fig. 5 (a) Normalized emission (λ_{ex} = 290 nm) spectra and (b) decay curves (λ_{ex} = 290 nm, λ_{em} = 354 nm) of Ce^{3+} in $K_{1.001}Sr_{0.998}Ce_{0.001}PO_4$ at different temperatures; the inset of (b) represents the temperature-dependent decay times of Ce^{3+}.

Fig. 5. displays the normalized emission (λ_{ex} = 290 nm) spectra and the decay curves (λ_{ex} = 290 nm, λ_{em} = 354 nm) of sample $K_{1.001}Sr_{0.998}Ce_{0.001}PO_4$ at different temperatures. From 78 to 500 K, the emission band shows a bit of short-wavelength shifting, because of the lattice expansion resulted weaker crystal field strength at higher temperatures. Moreover, the intensities of Ce^{3+} 5d_1-^2F_J (J = 5/2, 7/2) transitions decrease gradually, and the high-energy 5d_1-$^2F_{5/2}$ emission reduces relatively faster than the low-energy 5d_1-$^2F_{7/2}$ as seen in Fig. 5 (a). This is due to the enhanced reabsorption at higher temperatures as illustrated in ESI Fig. S5†. Meanwhile, two partial-resolved emissions become more overlapped because of the thermal-broadening of both bands. All decay curves in Fig. 5 (b) show exponential properties and no shortening lifetime with rising temperature, implying that the thermal quenching of Ce^{3+} emission does not occur yet. Instead, the slight increase of Ce^{3+} decay time can be observed in the inset of Fig. 5 (b). In consideration of the self-absorption at higher temperature, the lifetime of Ce^{3+} can be slightly lengthened.[30]

3.3. Luminescence of Eu^{3+} in $KSrPO_4$ and Construction of the VRBE Scheme

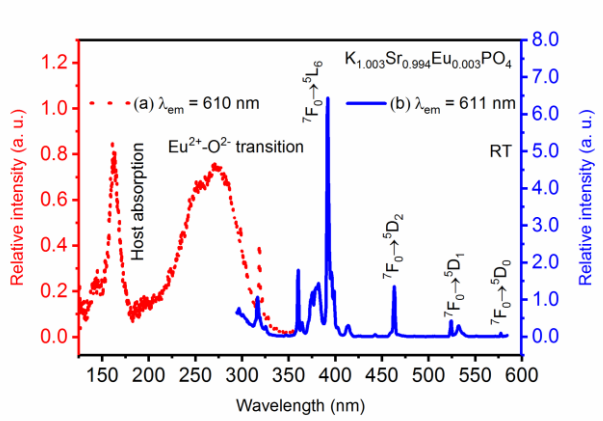

Fig. 6 Synchrotron radiation VUV-UV excitation spectrum (a, λ_{em} = 610 nm) and laboratory UV-vis excitation spectrum (b, λ_{em} = 611 nm) of $K_{1.003}Sr_{0.994}Eu_{0.003}PO_4$ sample at RT.

Fig. 6 displays the synchrotron radiation VUV-UV excitation spectrum (a, λ_{em} = 610 nm) and laboratory UV-vis excitation spectrum (b, λ_{em} = 611 nm) of $K_{1.003}Sr_{0.994}Eu_{0.003}PO_4$ sample at RT. The peak position and band shape of the high energy excitation band (162 nm, 7.65 eV) is the same with that in Fig. 3, and this band definitely corresponds to the excitonic absorption of this phosphate host. For the electron and hole binding energy in the exciton we will assume a value of $0.008(E^{ex})^2$ as proposed in refrence.[31] Accordingly, the bottom of the conduction band is estimated about 7.65 + 0.47 = 8.12 eV higher than the top of the valence band. The intense broad excitation band at about 272 nm (4.56 eV) is assigned to the Eu^{3+}-O^{2-} charge transfer transition. A series of sharp lines due to the f-f transition of Eu^{3+} can be observed below 300 nm.

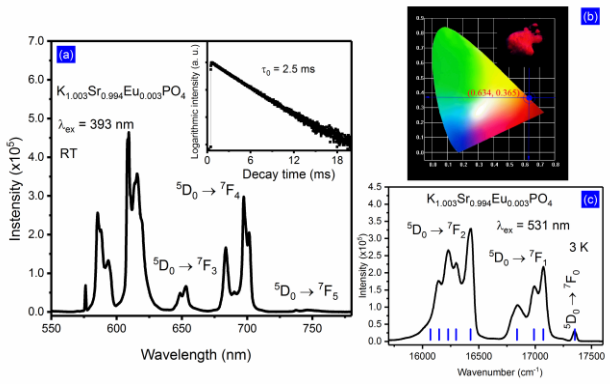

Fig. 7 (a) Emission spectrum (λ_{ex} = 393 nm) of $K_{1.003}Sr_{0.994}Eu_{0.003}PO_4$ sample at RT. The inset shows the decay curve (λ_{ex} = 393 nm, λ_{em} = 611 nm) of Eu^{3+} in $K_{1.003}Sr_{0.994}Eu_{0.003}PO_4$; (b) CIE chromaticity diagram for $K_{1.003}Sr_{0.994}Eu_{0.003}PO_4$ excited at 393 nm, the inset shows the digital photograph of $K_{1.003}Sr_{0.994}Eu_{0.003}PO_4$ upon 365 nm UV lamp excitation; (c) detailed emission spectrum (λ_{ex} = 531 nm) of $K_{1.003}Sr_{0.994}Eu_{0.003}PO_4$ sample at 3 K.

Fig. 7 (a) shows the emission spectrum (λ_{ex} = 393 nm) of $K_{1.003}Sr_{0.994}Eu_{0.003}PO_4$ at RT, which contains a series of 4f intra-configurational transitions from the excited $^5D_0$ level to ^7F_J (J = 0, 1, 2, 3, 4 and 5) and the strongest emission is $^5D_0$-$^7F_2$ transition with a maximum at 609.3 nm. The emission intensity of $^5D_0$-$^7F_2$ transition is hypersensitive to the Eu^{3+} micro-environment and depends closely on the point symmetry of Eu^{3+} site. The occurrence of the dominant $^5D_0$-$^7F_2$ transition indicates that Eu^{3+} ion is incorporated into a site without inversion symmetry. The main $^5D_0$-$^7F_2$ transition together with strong $^5D_0$-$^7F_4$ transition results in the deep-red luminescence of $K_{1.003}Sr_{0.994}Eu_{0.003}PO_4$ phosphor with CIE chromaticity coordinates (0.634, 0.365) as exhibited in Fig. 7 (b). Meanwhile, the lifetime is measured to be 2.5 ms as shown in the inset of Fig. 7 (a).

Provided that Eu^{3+} ions occupy Sr^{2+} sites with C_s point symmetry, the degeneracy of each $^7F_{0,1,2}$ multiplet of Eu^{3+} would be completely lifted. To verify the site symmetry of Eu^{3+} in $KSrPO_4$, in Fig. 7 (c) we give a more detailed emission spectrum of sample $K_{1.003}Sr_{0.994}Eu_{0.003}PO_4$ in the 15750-17500 cm^{-1} range, which is measured with step size 0.05 nm under the 531 nm $^7F_0$-$^5D_1$ transition excitation at 3 K. Since the $^5D_0$-$^7F_0$ transition will not be split, it can be used to determine the number of sites occupied. The single weak sharp line at 17350 cm^{-1} of the $^5D_0$-$^7F_0$ transition confirms one specific Eu^{3+} site occupation in $KSrPO_4$. Three emission lines in 16715-17160 cm^{-1} range are the results of magnetic-dipole $^5D_0$-$^7F_1$ transitions, and the lines in the range from 15850 to 16550 cm^{-1} are ascribed to the electric-dipole $^5D_0$-$^7F_2$ transitions. The $^5D_0$-$^7F_2$ emission splits into four clear lines and one line trailing in the low wavenumber side, in agreement with the substitution of Sr^{2+} sites with C_s point symmetry. In addition, it is reported that the intensity ratio of $^5D_0$-$^7F_0$ transition to $^5D_0$-$^7F_2$ transition commonly gives information on the magnitude of the J-mixing effect associated with the $^5D_0$-$^7F_0$ transition.[32] The very small ratio (0.013) in the present case suggests that the J-mixing effect can be neglected.

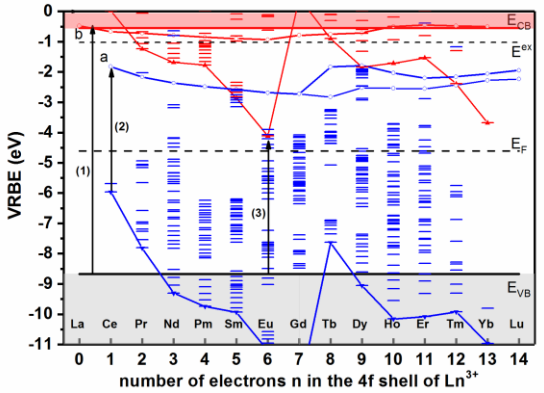

Fig. 8 Vacuum referred binding energy scheme for all lanthanide 4f (bar) and 5d (circle) states in $KSrPO_4$. Curve a connects the lowest 5d state of trivalent lanthanide and curve b that of the lowest 5d state of divalent lanthanide.

Fig. 8 displays the vacuum referred binding energy (VRBE) scheme for all lanthanide 4f and 5d states in $KSrPO_4$. The following required experimental data were used: band gap energy (~8.12 eV, see arrow 1); energies of the 4f-$5d_1$ transitions of Ce^{3+} (~4.14 eV, see arrow 2) and the 5d centroid energy shift (ε_c, ~1.19 eV) of Ce^{3+} in $KSrPO_4$; the Eu^{3+}-O^{2-} charge transfer energy in $KSrPO_4$ (~4.56 eV, see arrow 3).

To construct this VRBE scheme, the Coulomb repulsion energy U, which is the energy difference between the ground state 4f-shell electron binding energies $E_{4f}(Eu^{2+})$ in Eu^{2+} and $E_{4f}(Eu^{3+})$ in Eu^{3+}, is first estimated to be about 7.09 eV from the observed Ce^{3+} 5d centroid shift ε_c (1.19 eV) using Eq. (1), then the energy of Eu^{2+} ground state $^8S_{7/2}$ in the VRBE scheme is evaluated to be -4.11 eV based on Eq. (2).[20]

$$U = 5.44 + 2.834e^{-\varepsilon_c/2.2} \quad (1)$$

$$E_{4f}(Eu^{2+}) = -24.92 + \frac{18.05 - U}{0.777 - 0.0353U} \quad (2)$$

Therefore, the Eu^{3+} ground state $^7F_0$ is about -11.20 eV in VRBE. The 4f ground state energies of other Ln^{2+} and Ln^{3+} are determined using the most recently reported energy differences of Eu^{2+} / Eu^{3+} and Ln^{2+} / Ln^{3+} in refrence.[31] Then all 4f energies of Ln^{2+} and Ln^{3+} can be drawn in the VRBE scheme according to Dieke diagram.

After we obtain the 4f ground state ($^2F_{5/2}$) energy of Ce^{3+} about -5.96 eV in VRBE scheme, the Ce^{3+} $5d_1$ state can be derived to be approximately -1.82 eV by adding the observed energy of 4f-$5d_1$ transition (4.14 eV, see in Fig. 3). The lowest 5d energies of other Ln^{3+} can be determined with the known energy differences of Ce^{3+} and Ln^{3+}.

The 4f-$5d_1$ transition energy of Eu^{2+} (~3.16 eV) is measured experimentally as show in Fig. 10 or estimated from that of Ce^{3+}.[20] Hence the $5d_1$ energy of Eu^{2+} in VRBE scheme is determined to be -0.95 eV and the $5d_1$ energies of other Ln^{2+} are obtained from the energy differences of Eu^{2+} and Ln^{2+}.

The top of valence band energy of $KSrPO_4$ in VRBE scheme is estimated be -8.67 eV by subtracting Eu^{3+}-O^{2-} charge transfer energy (4.56 eV) from $E_{4f}(Eu^{2+})$ (-4.11 eV).[33] Subsequently, the bottom of conduction band (CB) energy of $KSrPO_4$ in VRBE scheme is -0.55 eV after adding the band gad energy (8.12 eV) of $KSrPO_4$.

Based on the VRBE scheme, the energy difference between the energy level of Ce^{3+} $5d_1$ state and the bottom of conduction band is approximately 1.27 eV. The activation energy (ΔE) of thermal quenching of Ce^{3+} 5d-4f luminescence generally corresponds to the energy required to raise an electron from the relaxed $5d_1$ excited level into the host conduction band.[34] This large energy gap explains that luminescence of Ce^{3+} doped $KSrPO_4$ phosphor possesses a good thermal stability.

3.4. The f-d Transitions of Pr^{3+} in $KSrPO_4$

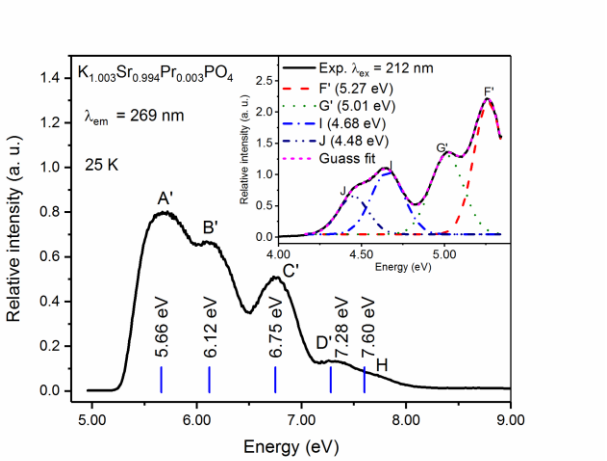

Fig. 9 Synchrotron radiation VUV-UV excitation spectrum (λ_{em} = 269 nm) of sample $K_{1.003}Sr_{0.994}Pr_{0.003}PO_4$ at 25 K; the inset shows the emission spectrum (λ_{ex} = 213 nm) at 25 K and the corresponding Gaussian fitting results.

Fig. 9 shows the synchrotron radiation VUV-UV excitation spectrum of samples $K_{1.003}Sr_{0.994}Pr_{0.003}PO_4$ at 25 K with four distinct bands (A', B', C', and D'). The lowest energy band is at 5.66 eV, which corresponds to the lowest 4f-5d transition of Pr^{3+}. The energy is consistent with that read from the VRBE scheme (5.64 eV). Since the CFS is almost the same for the 5d energy of Ce^{3+} as for Pr^{3+}, then the other four 4f-$5d_i$ (i = 2, 3, 4, 5) transitions of Pr^{3+} in $K_{1.003}Sr_{0.994}Pr_{0.003}PO_4$ are expected at 6.12, 6.75, 7.28, and 7.60 eV, respectively. Except for the last one (the highest $5d_5$ level), other four 5d multiplets are below the bottom of CB. The $5d_{1\text{-}3}$ states have larger energy gaps to the bottom of CB, and these three transitions are clearly observed in the excitation spectra.

In the inset of Fig. 9, we can find four emission bands in the range of 4.0-5.3 eV. These bands are attributed to the transitions from the lowest 5d state of Pr^{3+} terminating on $^3H_4$ (band F': 5.27 eV), $^3H_5$ (band G': 5.01 eV), $^3F_2$ (band I: 4.68 eV), and $^3F_4$ (band J: 4.48 eV).[35] Therefore, the Stokes shift of Pr^{3+} is approximately 0.39 eV, which coincides with that of Ce^{3+} (0.39 eV). The height-normalized VUV excitation (λ_{em} = 269 nm) and emission spectra (λ_{ex} = 213 nm) of samples $K_{1+x}Sr_{1-2x}Pr_xPO_4$ (x = 0.003, 0.007, 0.011) at 25 K are plotted in ESI Fig. S6†, showing that the f-d transitions of Pr^{3+} and Ce^{3+} have similar concentration-dependent luminescence properties including the shift of 4f-$5d_1$ excitation, the positions of zero phonon line (ZPL) and the self-absorption effect.

3.5. The Redox Properties of Eu in $KSrPO_4$

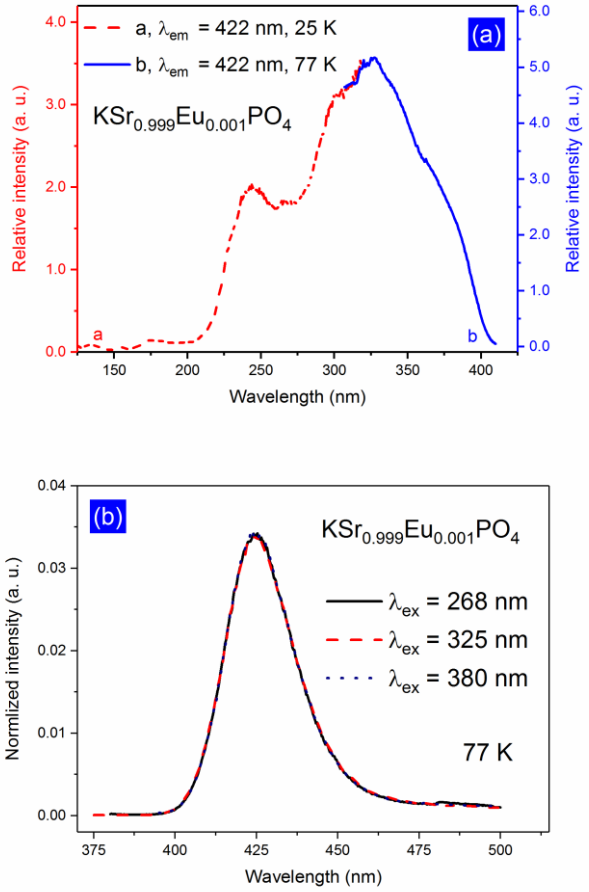

Fig. 10 (a) Synchrotron radiation VUV-UV excitation (curve a, λ_{em} = 422 nm, 25 K) and laboratory UV-vis excitation (curve b, λ_{em} = 422 nm, 77 K) spectra of sample $KSr_{0.999}Eu_{0.001}PO_4$, respectively; (b) normalized emission spectra (77 K) of $KSr_{0.999}Eu_{0.001}PO_4$ sample prepared in CO ambiance.

Fig. 10 displays the synchrotron radiation VUV-UV excitation (curve a) and laboratory UV-vis excitation (curve b) and emission spectra of sample $KSr_{0.999}Eu_{0.001}PO_4$ prepared in CO ambiance. Considering that in the 370-470 nm range there is no Eu^{3+} emission as shown in Fig. 10 (b), the excitation profile contains only the weak host-related absorption in short-wavelength range and the 4f-5d transitions of Eu^{2+} in the long-wavelength range when the emission wavelength of 422 nm is monitored. The lowest $4f^7$-$4f^6$5d excitation band in our case is about 392 nm (3.16 eV), which is empirically estimated as the energy at 15% to 20% of the maximum excitation intensity on the long-wavelength side.[36] This is close to the ZPLs position (~396 nm) as shown in ESI Fig. S7†. Referring to the VRBE scheme (Fig. 8), the energy barrier for electrons from excited state of Eu^{2+} to the bottom of conduction band (ΔE) is estimated to be 0.40 eV. A small ΔE energy usually makes the Eu^{2+} emission prone to thermal quenching by means of the ionization of the 5d electrons. The large ΔE value in present case implies a good thermal stability of luminescence of Eu^{2+} in $KSrPO_4$. The temperature-dependent decay dynamics in Fig. 11 confirms this standpoint, the thermal quenching of Eu^{2+} luminescence does not occur until 500 K.

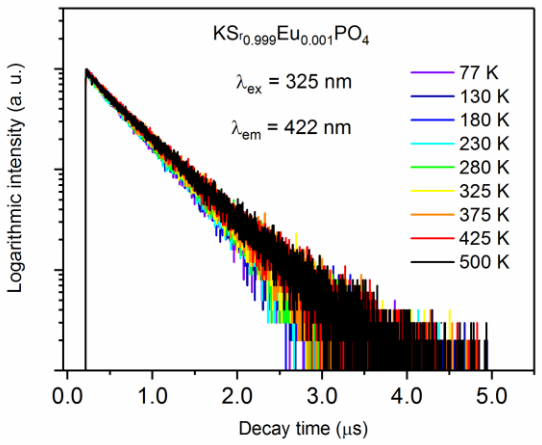

Fig. 11 Temperature dependent decay curves (λ_{ex} = 325 nm, λ_{em} = 422 nm) of $KSr_{0.999}Eu_{0.001}PO_4$ sample prepared in CO ambiance.

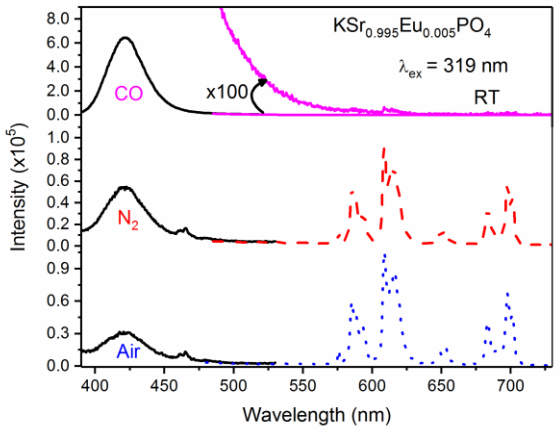

Fig. 12 Emission spectra (λ_{ex} = 319 nm) of $KSr_{0.995}Eu_{0.005}PO_4$ samples synthesized in CO (top), N_2 (middle) and air (bottom) conditions

Fig. 12 show emission spectra of $KSr_{0.995}Eu_{0.005}PO_4$ prepared in CO reducing, N_2 inert and air oxidizing conditions. We selected 319 nm as excitation wavelength because both Eu^{3+} and Eu^{2+} absorb at this wavelength [see Fig. 6 and 10 (a)]. In Fig. 12, the broad band at 425 nm belongs to d-f emission of Eu^{2+} and several sharp lines in long-wavelength correspond to Eu^{3+} f-f emission. Apparently, Eu^{3+} can be reduced to Eu^{2+} in CO reducing, N_2 inert, and air oxidizing conditions, but the reduction degrees are different. To express the degree of reduction of Eu^{3+} at these conditions, we calculated the ratios (A_2/A_3) of the integrated area of emission between 380-450 (A_2) and between 550-730 (A_3) nm, respectively. The results are 99.8/0.02 (CO), 46.4/53.6 (N_2), 31.9/68.1 (air), implying that the reduction degree decreases from CO to N_2 and air. When prepared in CO condition, it dominantly displays Eu^{2+} emission, and Eu^{3+} emission is very weak. For further demonstration, under excitation in the charge transfer band of Eu^{3+} (272 nm), the emission spectra of representative $KSr_{1-x}Eu_xPO_4$ (x = 0.001, 0.009 and 0.015) samples annealing in CO

condition are shown in ESI Fig. S8†, indicating Eu^{2+} ions are dominant. In N_2 and air conditions, Eu^{2+} emission dramatically decreases but is still present, showing that Eu^{3+} is partially reduced to Eu^{2+}, and it seems that more Eu^{3+} ions are reduced to Eu^{2+} when prepared under N_2 conditions.

The redox behaviour of Eu in $KSr_{0.995}Eu_{0.005}PO_4$ can be understood with the VRBE scheme in Fig. 8 when we consider that the redox properties of Eu ions are related to the Fermi energy position. The Fermi energy level locates midway the bottom of the CB and the top of the valence band (VB) when the phosphor is synthesized in inert atmosphere or near -4.06 eV (black dot curve) in the VRBE scheme. Eu ions usually prefer the divalent state when the ground state of Eu^{2+} is near or below the Fermi energy, and becomes more stable when it is further below the Fermi energy level. Referring to VRBE scheme, it is almost same as the Fermi energy level for $KSr_{0.995}Eu_{0.005}PO_4$ sample annealed in N_2, so Eu^{3+} can be partially reduced to Eu^{2+} in N_2. Fermi energy position somewhat increase or decrease at oxidizing or reducing conditions in comparison with that at inert condition. As a result, the reduction degree of Eu^{3+} increases in CO reducing condition but decreases in air oxidizing condition. On the other hand, when we consider the structure of the host compound, the stabilization of Eu^{2+} would relate to the similar ionic radii of Sr^{2+} and Eu^{2+}, and the rigid tetrahedral three-dimensional PO_4^{3+} groups as previous comments.[5,37]

4. Conclusions

We investigated the synchrotron radiation VUV-UV excitation spectra and corresponding emission spectra of Ln-doped $KSrPO_4$ (Ln = Ce^{3+}, Eu^{3+}, Eu^{2+}, Pr^{3+}) phosphors prepared by a high-temperature solid-state reaction method. It is found that five 4f-5d transitions of Ce^{3+} are at ~4.14, 4.60, 5.23, 5.76 and 6.08 eV, respectively. The energy of the Eu^{3+}-O^{2-} charge transfer state is found at 4.56 eV (272 nm), and the mobility band gap of $KSrPO_4$ is estimated to be 8.12 eV. Accordingly, the VRBE scheme is constructed and applied to understand the excellent thermally stable luminescence of Ce^{3+} and Eu^{2+}, 4f-5d transitions of Pr^{3+}, and redox properties of $Eu^{2+/3+}$.

The energy differences between the lowest 5d states of Ce^{3+} / Eu^{2+} and the bottom of the conduction band are read about 1.27 / 0.40 eV from VRBE scheme, individually. Referring to the experimental data and derived energy barriers, the 5d-4f luminescence of Ce^{3+} and Eu^{2+} has a good thermal stability and the thermal quenching does not occur as far as 500 K. In terms of the VRBE scheme, the lowest 5d energy of Pr^{3+} is evaluated to be about 5.64 eV, which is in good line with the experimental observation (5.66 eV), and other four 5d orbital of Pr^{3+} are with energies approximately 6.12, 6.75, 7.28, and 7.60 eV, respectively. Eu^{3+} can be reduced to Eu^{2+} in CO reducing, N_2 inert, and air oxidizing conditions, respectively. The reduction is almost totally in CO reducing ambiance, while that is partially in N_2 inert and air oxidizing atmosphere. From the viewpoint of host structure, the similar ionic radii of Sr^{2+} and Eu^{2+}, and the rigid tetrahedral three-dimensional PO_4^{3+} groups may be responsible for the phenomenon. From the standpoint of energy, this may relate to nearly same energies of Eu^{2+} ground state and the Fermi level of $KSrPO_4$ in neutral condition.

Conflicts of interest

There are no conflicts to declare.

Acknowledgements

The work has been financially supported by the National Natural Science Foundation of China (U1432249, U1632101 and 21671201), and the Science and Technology Project of Guangdong Province (2017A010103034).

Notes and references

1 N. Guo, H. P. You, C. Z. Jia, R. Z. Ouyang and D. H. Wu, *Dalton Trans.*, 2014, **43**, 12373.
2 Z. P. Ci, M. D. Que, Y. R. Shi, G. Zhu and Y. H. Wang, *Inorg. Chem.,* 2014, **53**, 2195.
3 X. Chen, Z. G. Xia and Q. L. Liu, *Dalton Trans.,* 2014, **43**, 13370.
4 W. G. Xiao, D. Wu, L. L. Zhang, X. Zhang, Z. D. Hao, G. H. Pan, L. G. Zhang, X. W. Ba and J. H. Zhang, *Inorg. Chem.,* 2017, **56**, 9938.
5 M. Y. Peng, Z. W. Pei, G. Y. Hong and Q. Su, *J. Mater. Chem.,* 2003, **13**, 1202.
6 M. Y. Peng, Z. W. Pei, G. Y. Hong and Q. Su, *Chem. Phys. Lett.,* 2003, **371**, 1.
7 P. Dorenbos, *Chem. Mater.,* 2005, **17**, 6452.
8 A. Bessiere, P. Dorenbos, C. Eijk, K. Krämer, H. Güdel, C. Donega and A. Meijerink, *Nucl. Instr. Meth. Phys. Res. A,* 2005, **537**, 22.
9 M. Alekhin, J. Haas, I. Khodyuk, K. Krämer, P. Menge, V. Ouspenski and P. Dorenbos, *Appl. Phys. Lett.,* 2013, **102**, 161915.
10 Y. T. Wu, L. Boatner, A. Lindsey, M. Zhuravleva, S. Jones, J. Auxier, H. Hall and C. Melcher, *Cryst. Growth Des.,* 2015, **15**, 3929.
11 W. J. Zhou, D. J. Hou, F. J. Pan, B. B. Zhang, P. Dorenbos, Y. Huang, Y. Tao and H. B. Liang, *J. Mater. Chem. C,* 2015, **3**, 9161.
12 Y. H. Wang, M. G. Brik, P. Dorenbos, Y. Huang, Y. Tao and H. B. Liang, *J. Phys. Chem. C,* 2014, **118**, 7002.
13 Y. S. Tang, S. F. Hu, C. C. Lin, N. Bagkar and R. S. Liu, *Appl. Phys. Lett.,* 2007, **90**, 151108.
14 C. C. Lin, R. S. Liu, Y. S. Tang and S. F. Hu, *J. Electrochem. Soc.,* 2008, **155**, J248.
15 Y. M. Peng, Y. K. Su and R. Y. Yang, *Opt. Mater.,* 2013, **35**, 2102.
16 A. A. Coelho, TOPAS Academic, Version 4; Coelho Software: Brisbane, Australia, 2005.
17 H. H. Lin, D. J. Hou, L. Li and H. B. Liang, *Dalton Trans.,* 2013, **42**, 12891.
18 Z. Xia and Q. Liu, *Prog. Mater. Sci*., 2016, **84**, 59.
19 Z. Xia, Z. Xu, M. Chen and Q. Liu, *Dalton Trans.*, 2016, **45**, 11214.
20 R. D. Shannon, *Acta Crystallogr., Sect. A,* 1976, **A32**, 751.
21 P. Dorenbos, *J. Lumin.,* 2013, **135**, 93.
22 C. H. Huang, T. M. Chen and B. M. Cheng, *Inorg. Chem.,* 2011, **50**, 6552.

23 L. Pieterson, M. Reid, R. Wegh, S. Soverna and A. Meijerink, *Phys. Rev. B,* 2002, **65**, 045113.
24 H. B. Liang, J. Wang, X. Ye, Z. F. Tian, H. H. Lin, Q. Su, Y. Tao, J. H. Xu, Y. Huang, G. B. Zhang and Y. B. Fu, *J. Alloys. Compd*., 2006, **425**, 307.
25 H. B. Liang, H. H. Lin, G. B. Zhang, P. Dorenbos and Q. Su, *J. Lumin.,* 2011, **131**, 194.
26 R. Shi, M. M. Qi, L. X. Ning, F. J. Pang, L. Zhou, W. J. Zhou, Y. C. Huang and H. B. Liang, *J. Phys. Chem. C,* 2015, **119**, 19326.
27 Y. H. Wang, J. H. Zhang, D. J. Hou, H. B. Liang, P. Dorenbos, S. Sun and Y. Tao, *Opt. Mater.,* 2012, **34**, 1214.
28 Z. W. Zhang, J. W. Hou, J. Li, X. Y. Wang, X. Y. Zhu, H. X. Qi, R. Lv and D. J. Wang, *J. Alloys Compd.,* 2016, **682**, 557.
29 Q. Peng, C. M. Liu, D. J. Hou, W. J. Zhou, C. G. Ma, G. K. Liu, G. M. Brik, Y. Tao and H. B. Liang, *J. Phys. Chem. C,* 2016, **120**, 569.
30 V. Bachmann, C. Ronda and A. Meijerink, *Chem. Mater*., 2009, **21**, 2077.
31 P. Dorenbos, *Opt. Mater.,* 2017, **69**, 8.
32 O. L. Malta, W. M. Azevedo, E. A. Gouveia and G. F. De Sá, *J. Lumin.,* 1982, **26**, 337.
33 P. Dorenbos, *J. Lumin.,* 2005, **111**, 89.
34 J. Ueda, S. Tanabe and T. Nakanishi, *J. Appl. Phys.,* 2011, **110**, 053102.
35 E. Kolk, P. Dorenbos, A. Vink, R. Perego and C. Eijk, *Phys. Rev. B,* 2001, **64**, 195129.
36 P. Dorenbos, *J. Phys.: Condens. Matter.,* 2003, **15**, 575.
37 Z. W. Pei, Q. H. Zeng and Q. Su, *J. Phys. Chem. Solids,* 2000, **61**, 9.